Ultrafast all-optical modulation in silicon-based nanoplasmonic devices

A. Y. Elezzabi*, Z. Han, S. Sederberg, and V. Van

Department of Electrical and Computer Engineering, University of Alberta, Edmonton, Alberta, Canada, T6G 2V4
**elezzabi@ece.ualberta.ca*

Abstract: A five-layer silicon-based nanoplasmonic waveguiding structure is proposed for ultrafast all-optical modulation and switching applications. Ultrafast nonlinear phase and amplitude modulation is achieved via photo-generated free carrier dynamics in ion-implanted silicon using above-bandgap femtosecond pump pulses. Both an analytical model and rigorous numerical simulations of the structures have shown that a switching time of 5ps and an on-off contrast of 35dB can be achieved in these devices.

OCIS codes: (240.6680) Surface plasmons; (230.7400) waveguides, slab; (320.0320) Ultrafast optics, (320.7120) Ultrafast optics, ultrafast phenomena; (250.5403) Optoelectronics, plasmonics.

References and links

1. M. I. Brongersma and P. G. Kik, Surface Plasmon Nanophotonics, eds, Springer Series in Optical Sciences, Vol. 131 (Springer, 2007).
2. E. Ozbay, "Plasmonics: merging photonics and electronics at nanoscale dimensions," Science **311**(5758), 189–193 (2006).
3. E. Hendry, F. J. Garcia-Vidal, L. Martin-Moreno, J. G. Rivas, M. Bonn, A. P. Hibbins, and M. J. Lockyear, "Optical control over surface-plasmon-polariton-assisted THz transmission through a slit aperture," Phys. Rev. Lett. **100**(12), 123901 (2008).
4. E. Hendry, M. J. Lockyear, J. Gomez Rivas, L. Kuipers, and M. Bonn, "Ultrafast optical switching of the THz transmission through metallic subwavelength hole arrays," Phys. Rev. B **75**(23), 235305 (2007).
5. J. A. Dionne, K. Diest, L. A. Sweatlock, and H. A. Atwater, "PlasMOStor: a metal-oxide-Si field effect plasmonic modulator," Nano Lett. **9**(2), 897–902 (2009).
6. G. Gagnon, N. Lahoud, G. A. Mattiussi, and P. Berini, "Thermally Activated Variable Attenuation of Long-Range Surface Plasmon-Polariton Waves," J. Lightwave Technol. **24**(11), 4391–4402 (2006).
7. K. J. Chau, S. E. Irvine, and A. Y. Elezzabi, "A Gigahertz Surface Magneto-Plasmon Optical Modulator," IEEE J. Quantum Electron. **40**(5), 571–579 (2004).
8. K. F. MacDonald, Z. L. Samson, M. I. Stockman, and N. I. Zheludev, "Ultrafast active plasmonics," Nat. Photonics **3**(1), 55–58 (2008).
9. K. J. Chau, M. Johnson, and A. Y. Elezzabi, "Electron-spin-dependent terahertz light transport in spintronic-plasmonic media," Phys. Rev. Lett. **98**(13), 133901 (2007).
10. J. A. Dionne, L. A. Sweatlock, H. A. Atwater, and A. Polman, "Plasmon slot waveguides: towards chip-scale propagation with subwavelength-scale localization," Phys. Rev. B **73**(3), 035407 (2006).
11. S. Gupta, M. Y. Frankel, J. A. Valdmanis, J. F. Whitaker, G. A. Mourou, F. W. Smith, and A. R. Calawa, "Subpicosecond carrier lifetime in GaAs grown by molecular beam epitaxy at low temperatures," Appl. Phys. Lett. **59**(25), 3276–3278 (1991).
12. S. Gupta, J. F. Whitaker, and G. A. Mourou, "Ultrafast carrier dynamics in III-V semiconductors grown by molecular beam epitaxy at very low substrate temperatures," IEEE J. Quantum Electron. **28**(10), 2464–2472 (1992).
13. A. Y. Elezzabi, J. Meyer, M. K. Y. Hughes, and S. R. Johnson, "Generation of 1-ps infrared pulses at 10.6 μm by use of low-temperature-grown GaAs as an optical semiconductor switch," Opt. Lett. **19**(12), 898–900 (1994).
14. S. Gupta, P. K. Bhattacharya, J. Pamulapati, and G. Mourou, "Subpicosecond photoresponse of carriers in low-temperature molecular beam epitaxial $In_{0.52}Al_{0.48}$ As/InP," Appl. Phys. Lett. **57**(15), 1543–1545 (1990).
15. Y. Kostoulas, L. J. Waxer, I. A. Walmsley, G. W. Wicks, and P. M. Fauchet, "Femtosecond carrier dynamics in low-temperature-grown indium phosphide," Appl. Phys. Lett. **66**(14), 1821–1823 (1995).
16. L. F. Lester, K. C. Hwang, P. Ho, J. Mazurowski, J. M. Ballingall, J. Sutliff, S. Gupta, J. Whitaker, and S. L. Williamson, "Ultrafast long-wavelength photodetectors fabricated on low-temperature InGaAs on GaAs," IEEE Photon. Technol. Lett. **5**(5), 511–514 (1993).
17. K. F. Lamprecht, S. Juen, L. Palmetshofer, and R. A. Höpfel, "Ultrashort carrier lifetimes in H^+ bombarded InP," Appl. Phys. Lett. **59**(8), 926–928 (1991).

#111651 - $15.00 USD Received 20 May 2009; revised 11 Jun 2009; accepted 12 Jun 2009; published 17 Jun 2009

18. M. B. Johnson, T. C. McGill, and N. G. Paulter, "Carrier lifetimes in ion-damaged GaAs," Appl. Phys. Lett. **54**(24), 2424–2426 (1989).
19. A. Y. Elezzabi, J. Meyer, and M. K. Y. Hughes, "600 fs 10.6 μm infrared pulse generation with radiation-damaged GaAs reflection switch," Appl. Phys. Lett. **66**(4), 402–404 (1995).
20. F. E. Doany, D. Grischkowsky, and C. C. Chi, "Carrier lifetime versus ion-implantation dose in silicon on sapphire," Appl. Phys. Lett. **50**(8), 460–462 (1987).
21. P. A. Schumann, Jr., and R. P. Phillips, "Comparison of classical approximations to free carrier absorption in semiconductors," Solid-State Electron. **10**(9), 943–948 (1967).

1. Introduction

Unlike electronic devices which rely on conventional charge transport and operate at limited bandwidth, their photonic counterparts exhibit significantly higher operating speeds and perform at much lower power consumption. Replacing conventional electronic circuit chip components with reliable, high-speed nanoscale circuits has been one of the thrusts behind the emergence of the field of nanophotonics. Devices of superior performance to current electronic ones have been demonstrated. However, displacing the mature electronic technology requires alternatives that possess not only better performance, but also ease of integration with the existing devices and systems. Although early nanophotonic devices were analogous to bulk and integrated photonic devices, this field has continued to evolve, and a major contender for the next-generation nanophotonic systems has emerged [1]. Recently, it has come to light that the intriguing class of nanoplasmonic devices could potentially revolutionize information and communication technology [2].

Nanoplasmonics exploits the interaction of light waves with electrons on conductive metallic nanostructures via high electric field confinement and manipulation. Since the device architecture is fundamentally metal-based, it is envisioned that hybrid plasmonic-electronic devices can be integrated within the current electronic device architecture where the nanoscale metallic-dielectric waveguides allow for the transport of both electrical and optical signals simultaneously. The latter is of particularly great importance because as electronic components in a complementary metal–oxide–semiconductor (CMOS) processor approach several nanometers in size, optical nanoscale plasmonic waveguides are considered an alternative route for chip interconnects. However, while progress has been realized in the development of nanoplasmonic optical elements, to date the majority of such components are passive elements, where light signal manipulation is limited by geometry or size. In order to realize advanced active circuit architectures, there is a need for active modulators and switching components operating at ultrahigh bandwidths and low power utilization.

Recently, ultrafast control of THz radiation transmission through subwavelength metallic structures on a silicon substrate by above-bandgap excitation has been demonstrated [3–4]. Previous active plasmonic devices have relied on modulation of charge distributions in n^+-Si by application of electric fields [5], thermo-optic effects [6], or application of magnetic fields to surface magneto-plasmon waves in bismuth-substituted yttrium iron garnets [7]. Although modulation of plasmonic amplitude has been shown, the effects upon which these modulations were induced restrict their operation bandwidth. Since the response of the charge modulation in silicon to an applied electric field is, in principle, similar to that of CMOS devices, its inherent capacitance limits operation to a few gigahertz. Similarly, the response of the thermo-optic effect is constrained by thermal diffusivity where switching times have been in the millisecond regime, and the bandwidth of the magneto-surface plasmon modulator is constrained by the strength of the biasing magnetic field. A promising ultrafast active plasmonic effect based on modulation of the optical properties of an aluminum film has also been demonstrated [8].

Evidently, one of the major challenges in ultrafast active plasmonics is the ability to directly control the coherent plasmon oscillations via external stimulus. This stems from the fact that direct manipulation of the electron density distribution within the metal's conduction band is necessary. Unlike carriers in semiconductors, the free electron density in metals is

#111651 - $15.00 USD Received 20 May 2009; revised 11 Jun 2009; accepted 12 Jun 2009; published 17 Jun 2009

very high and the Fermi level is located high within the conduction band. Achieving any tangible ultrafast modulation of the metal's optical properties at low excitation power via external modulation of the density of states proves very challenging. Recently, a novel approach towards active plasmonics has been realized as a potential candidate for a new class of spinplasmonic devices [9]. Efficient modulation of the electron density in the metal's conduction band is achieved via the electron's quantum spin state. By altering the electron's spin state, and accordingly the plasmon's, at a ferromagnetic-nonmagnetic metal interface, it was shown that spin-polarized plasmon propagation velocity, amplitude, phase, and polarization can be actively controlled via the application of an external magnetic field.

While this rapid interest stems from recent advances showing promises of functional nanoplasmonic optical circuits and a variety of light guiding structures operating below the diffraction limit, implementation of nanoplasmonic technology in a workable optical architecture requires a realization of basic ultrafast active nanoplasmonic components such as switches, modulators, logic elements, and routers. Here, we propose a new platform for ultrafast all-optical active nanoplasmonic devices based on nonlinear optical free carrier generation and absorption in semiconductor-loaded plasmonic slot waveguides. The switching and modulation processes are based on femtosecond optical perturbation, via an above-bandgap radiation laser pulse, of the permittivity of an ultrafast lifetime semiconductor layer embedded within a waveguide. In this analysis, we explore a five-layer nanoplasmonic waveguiding configuration consisting of a metal-semiconductor-free space-semiconductor-metal waveguide. We show that the nanoplasmonic waveguide confinement results in strong enhancement of the associated optical field, and therefore, very strong interaction within the waveguide occurs over a short length scale of only a few micrometers. As an illustrative example, we will focus on the guided-wave analysis technique to demonstrate practical devices for performing ultra-wideband modulation and ultrafast switching of 1550 nm laser radiation. The analysis suggests that designs would offer unprecedented bandwidth - limited only by the duration of the excitation pulse and the carrier lifetime of the semiconductor - and modulation depth of ~35dB. Furthermore, since this switching process is nonresonant for the information optical carrier signal or pulse, the switching platform can be applied to a wide spectral range of infrared wavelengths provided that the signal photon's energy is below the bandgap of the semiconductor material. It is envisioned that the realization of such ultrafast all-optical nanoplasmonic components will serve to bring nanoplasmonics technology closer into the realm of information and communication technology by creating novel optical circuit elements.

2. The five-layer plasmonic slot waveguide

Consider a five-layer planar plasmonic waveguide structure as depicted in Figs. 1(a) - 1(c). The structure consists of a central free space region of thickness a sandwiched between two semiconducting layers each of thickness $d\left(=(b-a)/2\right)$. Unlike a conventional metal-insulator-metal plasmonic waveguide where there are only two metal-dielectric interfaces, the five-layer structure provides two additional air-semiconductor interfaces. This effectively introduces an extra field mode confinement parameter which can be used to vary the refractive index and the losses within the semiconductor layer to achieve enhanced on/off modulation ratios. Capping each semiconductor layer with a metal cladding layer allows for plasmonic modes to be guided through the device. To achieve an ultrahigh bandwidth operation, the choice of the semiconductor material is restricted to those possessing ultrafast carrier lifetimes. An excellent candidate for the material is ion implanted Si (II-Si) which not only exhibits an ultrafast recombination lifetime for the photogenerated carriers, but also allows for ease of integration with metallic thin films.

This analysis uses a guided-wave formalism to study the propagation characteristics in the plasmonic waveguide. While this structure may support a number of modes, only the lowest-

#111651 - $15.00 USD Received 20 May 2009; revised 11 Jun 2009; accepted 12 Jun 2009; published 17 Jun 2009

order TM even (symmetric) mode will be analysed. As will be shown later, the TM mode provides almost twice the power confinement in the silicon layers when compared to the TE mode, allowing for more efficient modulation of the field amplitude. Furthermore, the lowest-order mode is chosen because practically, it is the easiest to excite and is the least lossy. Thus, we seek to derive an analytical expression for the characteristic dispersion relation of this mode.

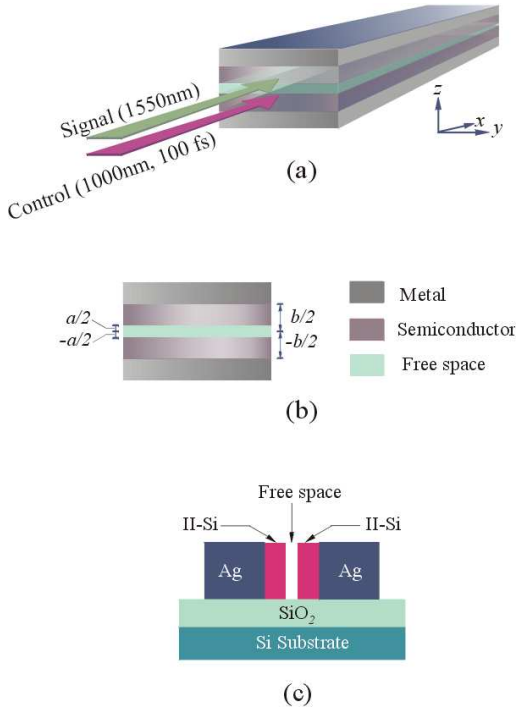

Fig. 1. (a) A schematic diagram showing the nanoplasmonic waveguide utilized as an ultrafast optical modulator and/or switch for infrared radiation. (b) The device has an air gap of thickness *a* and the overall distance between the two metal layers is *b*. (c) Depicts an embodiment of the device realized using ion implanted silicon (II-Si) and silver (Ag) layers fabricated on top of a silicon dioxide (SiO_2) layer and a silicon (Si) layers. The device can be fabricated using conventional metal and semiconductor deposition and etching techniques, whereas the free space region is fabricated via focused ion beam milling.

For the two dimensional planar waveguide with its propagation axis for a TM-polarized laser signal radiation along the *x*- direction, the temporal and spatial evolution of the light wave electric and magnetic fields are described by $e^{-i(\omega t-\beta x)}$, where ω is the frequency of the signal radiation and β is the complex propagation factor ($\beta = \beta_r + i\beta_i$). The light wave is assumed to be independent of the *y*-direction and thus for the TM polarization, the magnetic field, H_y can accordingly be described as: $H_y(x,y,z,t) = H_y(z)e^{-i(\omega t-\beta x)}$. For ease of experimental waveguide excitation, we consider only the lowest order even TM mode of H_y launched into the waveguide via end-fire coupling.

We commence the analysis by considering the five-layer waveguide, where the layers (i.e., free-space, semiconductor, and metal) are characterized by their intrinsic frequency-dependent complex permittivities and constant magnetic permeabilities. Hereafter, the following subscripts *f*, *s*, and *m*, refer to the free space, semiconductor, and metal regions, respectively. The characteristic TM mode wave Eq. describing the magnetic field is given by:

#111651 - $15.00 USD Received 20 May 2009; revised 11 Jun 2009; accepted 12 Jun 2009; published 17 Jun 2009

$$\frac{\partial H_y^2}{\partial z^2} + k_i^2 H_y = 0 \quad (i = f, s, m) \tag{1}$$

where $k_f^2 = \varepsilon_f k_0^2 - \beta^2$, $k_s^2 = \varepsilon_s k_0^2 - \beta^2$, and $k_m^2 = \beta^2 - \varepsilon_m k_0^2$ are the transverse wavevectors in the free space, semiconductor, and metallic regions, respectively; ε_f, ε_s, and ε_m are the relative permittivities of the free space, semiconductor, and metallic layers, respectively; and k_0 is the radiation wavevector in vacuum.

For a propagating even TM mode, we seek a general solution to the wave Eq. in the upper half space ($z \geq 0$) where the fields in both the free space gap and the semiconductor regions are of an oscillatory nature. Accordingly, we choose the following solution:

$$H_y(z) = \begin{cases} \cos k_f z, & z \in (0, \frac{a}{2}) \\ A\cos k_s z + B\sin k_s z, & z \in (\frac{a}{2}, \frac{b}{2}) \\ Ce^{-k_m z}, & z \in (\frac{b}{2}, +\infty), \end{cases} \tag{2}$$

where *A*, *B*, and *C* are magnetic field amplitude coefficients, and *a* and *b* define the bounds of the mode in the *z*-direction according to Fig. 1(b). It should be noted that the field distribution in the lower half space is symmetric and that this solution is general even in the case where $\beta_r^2 > \varepsilon_i k_0^2 (i = f, s)$ or $k_i (i = f, s)$ becomes imaginary. In this situation the mode distribution takes an exponential form describing surface modes.

Substituting the above solution of $H_y(z)$ into Maxwell's Eq. yields the following TM mode electric field components:

$$E_x(z) = \frac{-i}{\omega\varepsilon_0\varepsilon_i}\frac{\partial H_y}{\partial z} = \begin{cases} \frac{ik_f}{\omega\varepsilon_0\varepsilon_f} \sin k_f z, & z \in (0, \frac{a}{2}) \\ \frac{ik_s}{\omega\varepsilon_0\varepsilon_s}\left(A\sin k_s z - B\cos k_s z\right), & z \in (\frac{a}{2}, \frac{b}{2}) \\ \frac{ik_m}{\omega\varepsilon_0\varepsilon_m} Ce^{-k_m z}, & z \in (\frac{b}{2}, +\infty) \end{cases} \tag{3}$$

Next, by invoking the continuity of the tangential field components (i.e. H_y and E_x) at the two interfaces $z = a/2$ and $z = b/2$, we obtain the characteristic Eq. for the even TM mode:

$$\tan(k_f \frac{a}{2}) = \frac{k_m\varepsilon_f}{k_f\varepsilon_m} \frac{1 - \frac{k_s\varepsilon_m}{k_m\varepsilon_s}\tan(k_s \frac{b-a}{2})}{1 + \frac{k_m\varepsilon_s}{k_s\varepsilon_m}\tan(k_s \frac{b-a}{2})}. \tag{4}$$

In the present case, since the lossy metal and semiconductor layers are described by complex permittivities, Eq. (4), has a complex transcendental form, whose solutions give discrete values for the propagation factor, β, or the wavevectors k_f, k_s and k_m in the complex plane. Consecutive solution of the complex transcendental Eq. yields the propagation characteristics for the TM even mode. Notably, when the semiconductor layer thickness fills the free space gap (i.e. $a = 0$), the above dispersion relation reduces to

#111651 - $15.00 USD Received 20 May 2009; revised 11 Jun 2009; accepted 12 Jun 2009; published 17 Jun 2009

$$\tan(k_s \frac{b}{2}) = \frac{k_m \varepsilon_s}{k_s \varepsilon_m}, \quad (5)$$

as for a conventional metal-dielectric-metal waveguide [10].

The utilization of the aforementioned plasmonic waveguide structure as an ultrafast amplitude modulator or as a switch is as follows: When a TM-polarized laser signal radiation, whose photon energy, hv_{signal}, is less than the bandgap energy (E_g) of the semiconductor, is launched into the plasmonic waveguide, it propagates and only suffers losses due to the metallic layers as the semiconductor layers are transparent to the signal radiation. However, the optical properties, and particularly the losses, of the waveguide can be altered on an ultrafast time scale by the simultaneous co-propagation of a TE-polarized ultrashort laser pulse (hereafter referred to as the control pulse) whose photon energy $hv_{control} \geq E_g$. The choice of TE-polarization of the control pulse ensures long propagation distance, whereas the choice $hv_{control} \geq E_g$ ensures that free charge carriers (electron-hole (e-h) pairs) are photogenerated in the semiconductor layers. The transient photoinjection of the e-h pairs effectively modifies both the real and the imaginary refractive indices of the semiconductor layers. Once a high enough carrier density is produced, the plasmonic waveguide becomes too lossy to support the propagation of the signal radiation, resulting in significant attenuation at this wavelength. However, while the turn-off process is limited only by the duration of the ultrafast control pulse, which can be as short as a few femtoseconds, the turn-on mechanism, or the recovery time of the device, is limited by the recombination lifetime of the e-h pairs in the semiconductor layers. Nevertheless, the use of ultrafast carrier lifetime semiconductors, such as LT-GaAs [11–13], LT- $In_{0.52}Al_{0.48}$ [14], LT-InP [15], LT- InGaAs [16], H^+-implanted InP [17], H^+-implanted GaAs [18,19], or O^+ implanted Si [20], alleviates such a constraint. In the following investigation, we employ a signal laser radiation at a wavelength of 1550nm and a 100 fs ultrafast control laser pulse at a wavelength of 1000nm. For the metallic layers in the cladding regions, we chose silver metal with ε_m = -125.735 + 3.233i due to its low loss at 1550nm. The semiconductor layers consist of ion-implanted Si (II-Si). Implantation of 10^{13} cm^{-2} O^+ ions at both 200 keV and 100 keV into a Si semiconductor layer produces ultrafast recombination centers that reduce the carrier lifetime from τ_c ~100 ns to τ_c~1 ps [20].

Since the ultrafast response of the plasmonic modulator/switch is drawn into the model by incorporating the time-varying permittivity of the Si layers via $\beta(t)$, one must ensure that the temporal variation of $\varepsilon_s(t)$ occurs on time scales beyond a few optical cycles of the 1550 nm signal radiation such that the signal radiation experiences temporally homogeneous perturbations in the refractive index. Although the mode profile of the control pulse dictates the transverse distribution of free carriers in the silicon layers, the analysis may be simplified by assigning an average induced complex refractive index across the thin silicon layer. This assumption is consistent with the fact that the silicon layer thickness is much less than the control pulse wavelength and carrier diffusion occurs on a nanosecond timescale, such that during the switching process it can be taken as a constant. In determining the propagation of the control pulse along the *x*-direction, the spatial extent of the control radiation is evaluated from the following dispersion relation:

$$\tan(k_f \frac{a}{2}) = \frac{k_m}{k_f} \frac{1 - \frac{k_s}{k_m} \tan(k_s \frac{b-a}{2})}{1 + \frac{k_m}{k_s} \tan(k_s \frac{b-a}{2})} \quad (6)$$

for TE-polarized light. Equation (6) is obtained using a similar analysis employed in deriving the characteristic Eq. for the even TM mode (i.e. Equation (4)).

#111651 - $15.00 USD Received 20 May 2009; revised 11 Jun 2009; accepted 12 Jun 2009; published 17 Jun 2009

The dynamical permittivity of the semiconductor layers is characterized by the frequency-dependent Drude-Lorentz model for a semiconductor:

$$\varepsilon(t) = \varepsilon_b^{'}\left(1 - \frac{n(t)e^2}{\varepsilon_b^{'}\varepsilon_o m^* \omega^2}\frac{\omega^2\langle\tau\rangle^2}{1+\omega^2\langle\tau\rangle^2}\right) - i\varepsilon_b^{'}\left(\frac{\varepsilon_b^{''}}{\varepsilon_b^{'}} + \frac{n(t)e^2}{\varepsilon_b^{'}\varepsilon_o m^* \omega^2}\frac{\omega\langle\tau\rangle}{1+\omega^2\langle\tau\rangle^2}\right) \quad (7)$$

where, $\varepsilon_b^{'}$ = 11.8 and $\varepsilon_b^{''}$ = 9.2 × 10^{-4} are the intrinsic real and imaginary components of the background permittivity for Si which include the contribution of bound charges, ε_o is the free space permittivity, ω is the signal radiation frequency, e is the electronic charge, m^* is the free carrier effective mass, where $m^{*-1} = m_e^{*-1} + m_h^{*-1}$, with $m_e^* = 0.259m_o$ as the electron and $m_h^* = 0.38m_o$ as the hole effective masses, respectively, m_o is the electron mass, $\langle\tau\rangle$ = 10.6 fs is the average carrier-carrier relaxation time, and $n(t)$ is the photogenerated carrier density in the conduction band [21]. Both the real and imaginary parts of the permittivity, and, therefore, the refractive index of the semiconductor layers, are related to the density of the photogenerated e-h pairs (i.e. $n(t)$). For photoinjection of carriers at a density above a critical e–h density, n_c, corresponding to

$$n_c = \frac{\varepsilon_o\varepsilon_b^{'}m^*\omega^2}{e^2}\frac{1+\omega^2\langle\tau\rangle^2}{\omega^2\langle\tau\rangle^2} \quad (8)$$

the real part of the permittivity becomes negative, and the semiconductor layers behave as metal-like layers at the frequency ω. For silicon at the 1550nm signal radiation, n_c = 8.5 × 10^{20} cm^{-3}.

The time-varying properties of the photoinjected e-h carrier density is introduced by considering free-carrier generation from the 1000 nm, 100 fs $sech^2$ shaped control pulse and subsequent free-carrier decay through recombination of the e-h pairs at recombination centers in the II-Si layers. The resulting e-h carrier density as a function of time is obtained from the Eq.:

$$\frac{\partial n(t)}{\partial t} = \frac{n_o}{\tau_p}\sec h^2\left(\frac{t-t_o}{\tau_p}\right) - \frac{n(t)}{\tau_c}, \quad (9)$$

where n_0 is the carrier density at the peak of the excitation control pulse when $t = t_o$, τ_p = 100 fs is the control laser pulse duration, and τ_c = 1 ps is the carrier lifetime in the II-Si layers.

3. Results and discussion

Since the nanoplasmonic waveguide explored is a planar structure having an infinite extent in one direction, it is necessary to investigate the influence of field confinement along the *y*-direction on the mode within the waveguide. Such analysis is important for realizing and fabricating a functional nanoplasmonic device (shown in Fig. 1(b)) as it provides minimum waveguide width, *w*, where the analytical expressions for the fields and the characteristic Eqs. are applicable. To ascertain such analysis, it is necessary to evaluate the spatial distribution of time-averaged power, $\langle S\rangle$, for a finite width nanoplasmonic waveguide using the following expression

$$\langle S\rangle = \int_{-\infty}^{+\infty} \mathrm{Re}\left\{E_z H_y^*\right\}\, dz \quad (10)$$

where E_z and H_y^* are obtained from Eqs. (2) and (3) and compare it with the time-averaged power calculated from a finite element method numerical solution to Maxwell Eqs. for a wave

#111651 - $15.00 USD Received 20 May 2009; revised 11 Jun 2009; accepted 12 Jun 2009; published 17 Jun 2009

guide of finite width *w*. Figures 2(a) and 2(b) depicts the spatial distributions of $\langle S \rangle$ for 1550nm radiation within a five-layer waveguide consisting of Ag(100nm):II-Si(150nm):free space(50nm):II-Si(150nm):Ag(100nm) and a width of *w* = 300nm calculated using the two methods. The numerical solution is in good agreement with that obtained from Eq. (10) indicating that due to strong confinement of the radiation in the semiconductor layers, the model is also applicable for small waveguide widths. Figure 2(c) shows the 2D intensity distribution of the waveguide, from which the strong radiation confinement of the 1550nm radiation within the II-Si layers is evident.

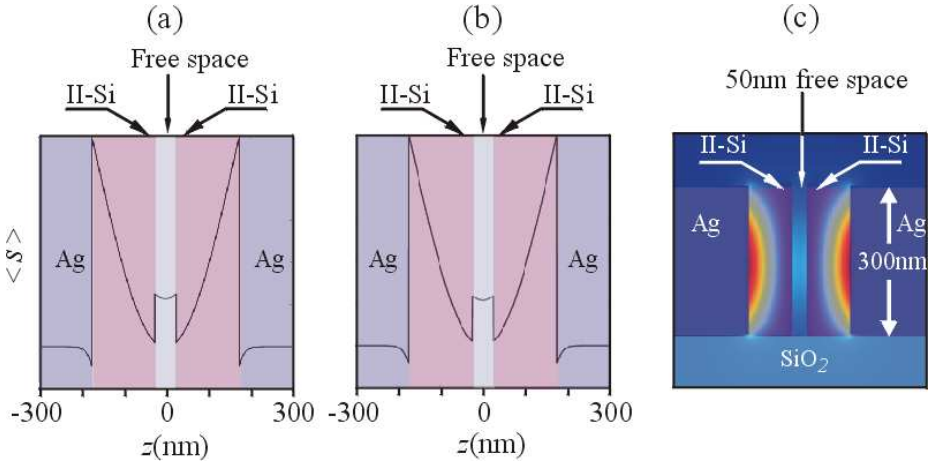

Fig. 2. (a) Spatial distribution of time-averaged power, <*S*> normalized to 1 W per unit width in the y-direction for 1550 nm radiation within a five layer waveguide consisting of Ag(100nm):II-Si(150nm):free space(50nm):II-Si(150nm):Ag(100nm) calculated using (a) the analytical model and (b) a finite element solution to Maxwell Eqs. The cross section is taken at the center of the waveguide in panel (c)). (c) The corresponding mode profile inside the waveguide calculated using finite element method numerical solution to Maxwell's Eqs.

When compared to the TM mode profile, it is found that the TE mode provides only 53% of the power confinement to the silicon layers. Since optical excitation modifies the waveguide attenuation and the TM mode confinement, it is necessary to examine the temporal evolution of both the real, $\eta_s(t)$, and imaginary, $\kappa_s(t)$, components of the refractive index of the semiconductor layers first. Notably, significant photoinjection of e-h pairs at a density *n*(t) $\geq n_c$ influences the TM mode propagation in a similar fashion as altering the semiconductor layers' thickness. Figure 3(a) presents the real and imaginary parts of the refractive index in the first 6 ps after excitation at various photoexcitation carrier densities ranging from n_0/n_c = 0.05 to 0.2 (i.e. (0.43 - 1.7) × 10^{20} cm^{-3}). The strong dependence on n_0/n_c, and thus on the control pulse intensity, is evident in both $\eta_s(t)$ and $\kappa_s(t)$. For example, at a representative value of excitation of n_0/n_c = 0.15, the peak of $\eta_s(t)$ has decreased by 13%, while $\kappa_s(t)$ has increased dramatically by two orders of magnitude from 10^{-4} to 3.76 × 10^{-2}. Both $\eta_s(t)$ and $\kappa_s(t)$ recover back to their initial values within 5 ps.

#111651 - $15.00 USD Received 20 May 2009; revised 11 Jun 2009; accepted 12 Jun 2009; published 17 Jun 2009

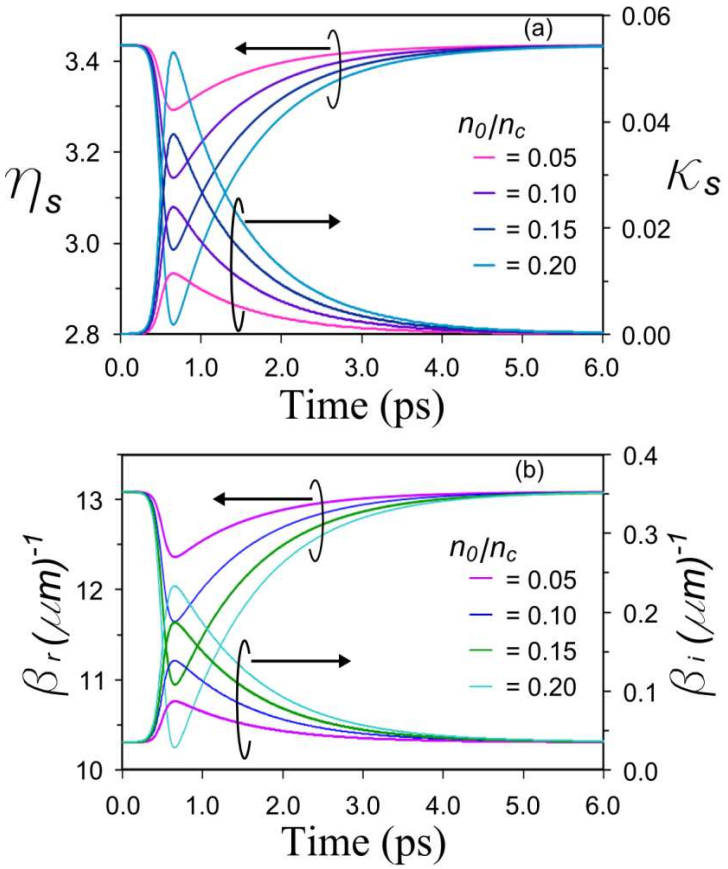

Fig. 3. (a) Real, $\eta_s(t)$, and imaginary, $\kappa_s(t)$, values of the refractive index in the first 6 ps after excitation at various photoexcitation carrier densities ranging from n_0/n_c = 0.05 to 0.2. (b) $\beta_r(t)$ and $\beta_i(t)$ at the same photoexcitation carrier density range from n_0/n_c = 0.05 to 0.2 calculated for the (a,d) = (50nm, 150nm) waveguide configuration.

Of particular interest are the phase, $\beta_r(t)$, and the attenuation, $\beta_i(t)$, constants of the waveguide at signal wavelength of 1550nm. The temporal evolution of these constants is determined by solving the dispersion relation (Eq. (4)) at the time instant during the evolution dynamics of n(t). However, since both $\beta_r(t)$ and $\beta_i(t)$ are strongly dependent on the waveguide dimensions, a and d, and on the density of the photoinjected carriers, n_0, in the following analysis, $\beta_r(t)$ and $\beta_i(t)$ are evaluated for the following representative sets of a and d values: (a,d) = (0nm, 150nm), (50nm, 150nm), and (100nm, 150nm). The configuration (a,d) = (0nm, 150nm) represents a three-layer metal-semiconductor-metal plasmonic waveguide. Figure 3(b) illustrates $\beta_r(t)$ and $\beta_i(t)$ in the first 6 ps at the same photoexcitation carrier density range from n_0/n_c = 0.05 to 0.2 for the case (a,d) = (50nm, 150nm). Generally, the time evolution of $\beta_r(t)$ and $\beta_i(t)$ exactly follows that of $\eta_s(t)$ and $\kappa_s(t)$, indicating that by using an II-Si having τ_c = 1 ps, the recovery time of the device is ~5 ps. A small perturbation to the II-Si layer permittivity manifests itself as an enhanced attenuation. Thus, by operating the plasmonic waveguide in transmission mode, the dominant effect on the modulated 1550nm radiation is amplitude attenuation resulting from free-carrier absorption due to $\beta_i(t)$.

#111651 - $15.00 USD Received 20 May 2009; revised 11 Jun 2009; accepted 12 Jun 2009; published 17 Jun 2009

While the plasmonic waveguide loss is activated with the application of an ultrafast control pulse, it is important to ensure that the device operates in the linear regime over a wide range of excitation intensities. With the aid of Fig. 4, this is better illustrated by plotting the minimum phase, $\beta_r^{\min}(t)$, and maximum attenuation, $\beta_i^{\max}(t)$ parameters for each set of (a,d) dimensions as a function of n_0/n_c. For waveguides (a,d) = (0nm,150nm), (50nm,150nm), and (100nm,150nm) and at a low photoinjected carrier density, $n_0/n_c \leq 0.1$, $\beta_r^{\min}(t)$ and $\beta_i^{\max}(t)$ vary linearly with n_0/n_c. Within $0.1 \leq n_0/n_c \leq 0.2$ the deviation from linearity is less than 12%. Hence, the range of operation is set to be below $n_0/n_c \leq 0.2$.

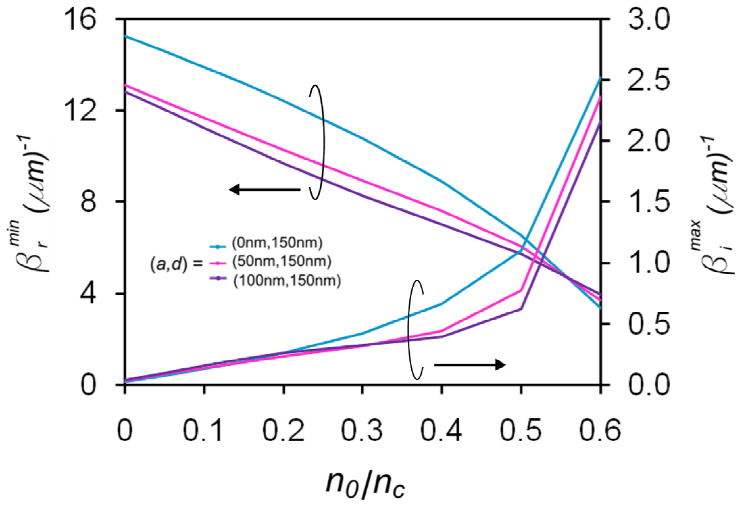

Fig. 4. Minimum phase, $\beta_r^{\min}$, and maximum attenuation, $\beta_i^{\max}$, parameters for each set of (a,d) dimensions as a function of n_0/n_c from 0 to 0.2, for the waveguides having (a,d) = (0nm,150nm), (50nm,150nm), and (100nm,150nm).

Notably, prior to turning on the 1000nm control pulse (i.e. $n_0/n_c = 0$), using the values for $\beta_i^{\max}(t=0)$, long propagation distances of 21.7μm, 14.2μm, and 13.2μm corresponding to (a,d) = (0nm,150nm), (50nm,150nm), and (100nm,150nm) plasmonic waveguides, respectively, are obtained. For the 1000nm control pulse wavelength, the propagation lengths are found to be 16.5 μm, 16.9μm, 16.3μm for the same order of the waveguides. Thus, to ensure that sufficient free carriers are excited throughout the device, one must choose the waveguide's length, $L \leq 16.5$ μm, 16.9μm, 16.3μm for each corresponding (a,d) waveguide set.

As the control pulse intensity increases beyond a critical value, the change in the intensity distribution of the mode along the transverse direction also changes. For illustrative purposes, we present the calculations using 2D-FDTD for the (a,d) = (50nm,150nm) plasmonic waveguide. Shown in Fig. 5 is the intensity distribution of the 1550nm light signal at three excitation electron densities of n_0/n_c = 0, 0.2, and 1.1. It should be noted that prior to excitation (n_0/n_c = 0), the 1550nm radiation propagates predominately in the II-Si layers as depicted in Fig. 5(a); however, for higher excitations ($n_0/n_c \geq 1.1$) the II-Si permittivity becomes metal-like and the mode propagates in the free space region only as shown in Fig. 5(c). In this situation, the semiconductor layers effectively 'disappear' and the waveguide properties mimic that of the metal-free space-metal waveguide described by Eq. (5). At the highest excitation density, n_0/n_c = 1.1, the attenuation constant at the peak of the control pulse (i.e at $t = t_0$) is 3.642μm^{-1}, yielding a propagation distance of only 137nm at 1550nm.

#111651 - $15.00 USD Received 20 May 2009; revised 11 Jun 2009; accepted 12 Jun 2009; published 17 Jun 2009

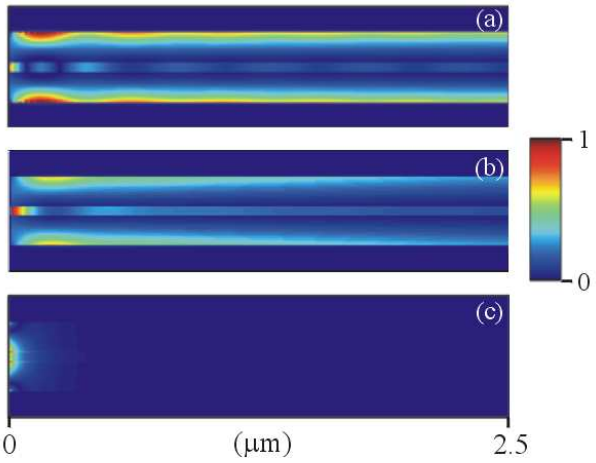

Fig. 5. FDTD intensity distribution of 1550nm signal laser at (a) $n_0/n_c = 0$, (b) $n_0/n_c = 0.2$, and (c) $n_0/n_c = 1.1$ for a Ag(100nm):II-Si(150nm): free space(50nm):II-Si(150nm):Ag(100nm) waveguide.

To demonstrate the ultrafast operation of the plasmonic waveguide as an ultrawide bandwidth amplitude modulator, we investigate three devices each of length $L = 15$ μm: (*i*) a three-layer Ag(100nm):II-Si(300nm):Ag(100nm) waveguide and (*ii*) two configurations of a five-layer waveguide: Ag(100nm): II-Si(150nm): free-space(50nm): Si(150nm): Ag(100nm) and Ag(100nm): II-Si(150nm): free-space(100nm): II-Si(150nm): Ag(100nm). Figures 6(a)-6(c) illustrate the normalized output intensity of the ultrafast plasmonic switch as a function of time for these three modulators. The modulators' responses are calculated at photoinjected carrier densities $n_0/n_c = 0$ (on state), 0.05, 0.1, 0.15, and 0.2. Assuming a 100% photon to electron generation quantum efficiency when the device is excited and waveguide dimensions of 300nm × 300nm × 15μm, the required energy per pulse in each case corresponds to 16.6pJ, 33.2pJ, 49.8pJ and 66.4pJ, respectively. It is evident from the Fig. that in response to the 1000nm control pulse excitation, the 1550nm signal intensity drops sharply from the 'on' to the 'off' state in ~100fs (following the rise time of the control pulse) and recovers back to the initial 'on' state within ~5ps. In order to assess the devices' performance, the '*on-off*' extinction ratios are calculated as a function of the photoinjected carrier densities as shown in Fig. 6(d). As expected from the increasing loss at high excitation, the extinction ratio increases with increasing photoinjected density. However, it is imperative to realize that the optimum operating conditions should combine the practicality of a low photoinjection carrier density (i.e. low control pulse energy) with the benefits of a high extinction ratio. At a maximum photoinjected density of $n_0/n_c = 0.2$, an extinction ratio of 30.3dB, is achieved using the three layer Ag(100nm):II-Si(300nm):Ag(100nm) waveguide. However, the Ag(100nm):II-Si(150nm):free-space(50nm):Si(150nm):Ag(100nm) and Ag(100nm):II-Si(150nm):free space(100nm):II-Si(150nm):Ag(100nm) waveguides exhibit extinction ratios of 30.6dB and 35.3dB, respectively. Higher extinction ratios may be obtained by increasing the density of the photogenerated e–h density at the expense of a higher energy budget. These extinction levels can be achieved in realistic devices fabricated via deposition and etching of ion implanted silicon and silver layers on top of a silicon dioxide layer. Finally, the free space region can be fabricated via focussed ion beam milling.

#111651 - $15.00 USD Received 20 May 2009; revised 11 Jun 2009; accepted 12 Jun 2009; published 17 Jun 2009

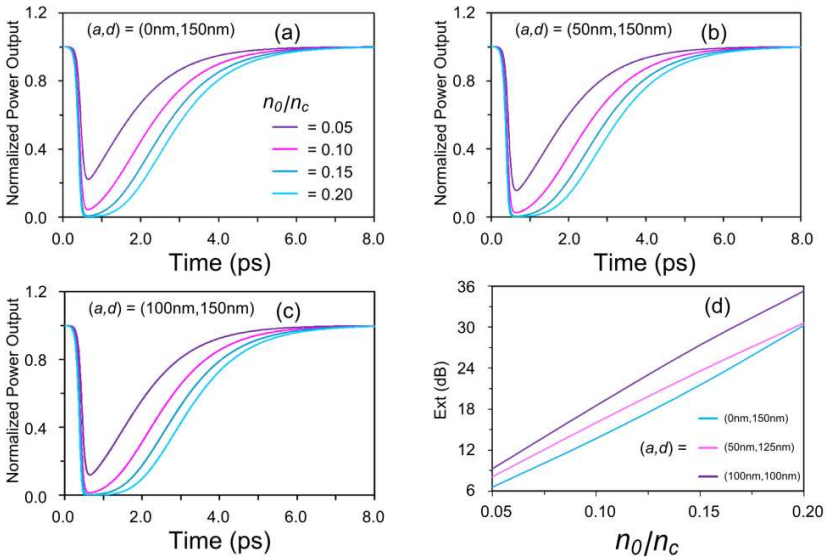

Fig. 6. (a) The normalized output intensity of the ultrafast plasmonic switch as a function of time for three modulators. (a) Ag(100nm):II-Si(300nm):Ag(100nm) waveguide, (b)Ag(100nm):II-Si(150nm):free space(50nm):II-Si(150nm):Ag(100nm), and (c) Ag(100nm):II-Si(150nm):free space(100nm):II-Si(150nm):Ag(100nm). Each waveguide modulator configuration is calculated for photoinjected carrier densities of n_0/n_c = 0 (on state), 0.05, 0.1, 0.15, and 0.2. (d) On-off extinction ratios are calculated as function of the photoinjected carrier densities for the same nanoplasmonic waveguides.

5. Conclusion

We investigated a novel platform for development of ultrafast all-optical active nanoplasmonic devices based on optical free carrier generation and absorption in five-layer silicon nanoplasmonic waveguide structures. The waveguide structures can be fabricated with standard thin-film waveguide fabrication processes and can be integrated with the existing nanophotonics device architectures. High field confinement at the silicon-metal interfaces together with ultrafast photoexcitation of the semiconductor layers results in enhanced single-photon absorption within the nanoplasmonics waveguide that leads to strong and ultrafast modulation of the signal beam. For applications to ultrafast switching and modulation, we have shown that the ultrahigh operation bandwidth is limited only by the duration of the control pulse and the carrier lifetime of the semiconductor layers. Furthermore, the off–on extinction ratio or modulation depth is sufficiently high at low optical excitation, enabling the generation of ultrashort laser pulses and modulation with an extremely high signal-to-background ratio. The conceived devices establish a new platform for development of active nanoplasmonics and offer promising prospects for realizing active devices for all-optical control of light.

Acknowledgments

This work was supported by the Natural Sciences and Engineering Research Council of Canada (NSERC) and the Canada Research Chairs (CRC) program.

#111651 - $15.00 USD Received 20 May 2009; revised 11 Jun 2009; accepted 12 Jun 2009; published 17 Jun 2009